Article

Mechanical Transfer of Black Phosphorus on a Silk Fibroin Substrate: A Viable Method for Photoresponsive and Printable Biomaterials

Martina Alunni Cardinali, Maria Rachele Ceccarini, Irene Chiesa, Silvia Bittolo Bon, Tommaso Rondini, Manuel Serrano-Ruiz, Maria Caporali, Silvia Tacchi, Alberto Verdini, Caterina Petrillo, Carmelo De Maria, Tommaso Beccari, Paola Sassi, and Luca Valentini*
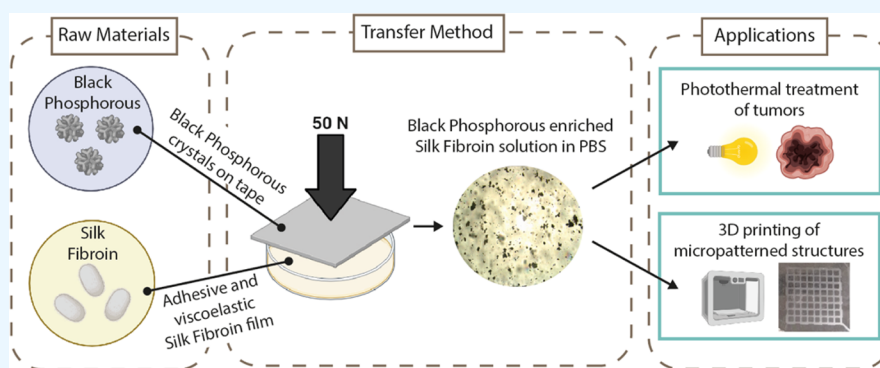
Read Online

ACCESS | Metrics & More | Article Recommendations | SI Supporting Information

ABSTRACT: Despite the technological importance of semiconductor black phosphorus (BP) in materials science, maintaining the stability of BP crystals in organic media and protecting them from environmental oxidation remains challenging. In this study, we present the synthesis of bulk BP and the exploitation of the viscoelastic properties of a regenerated silk fibroin (SF) film as a biocompatible substrate to transfer BP flakes, thereby preventing oxidation. A model based on the flow of polymers revealed that the applied flow-induced stresses exceed the yield stress of the BP aggregate. Raman spectroscopy was used to investigate the exfoliation efficiency as well as the environmental stability of BP transferred on the SF substrate. Notably, BP flakes transferred to the SF substrate demonstrated improved stability when SF was dissolved in a phosphate-buffered saline medium, and in vitro cancer cell viability experiments demonstrate the tumor ablation efficiency under visible to near-infrared (Vis−nIR) radiation. Moreover, the SF and BP-enriched SF (SF/BP) solution was shown to be processable via extrusion-based three-dimensional (3D) printing. Therefore, this work paves the way for a general method for the transferring of BP on natural biodegradable polymers and processing them via 3D printing toward novel functionalities and complex shapes for biomedical purposes.

INTRODUCTION

Black phosphorus (BP), a layered semiconducting material, has a band gap that varies from 0.3 eV for bulk materials to 2.0 eV for phosphorene (monolayer BP), thereby enabling[1−4] a broad range of applications in phototherapy.[5−7] The gold standard procedure to obtain BP nanoflakes for bioimaging and phototherapy[8,9] is the liquid exfoliation method; however, it has recently been demonstrated that BP nanoflakes with reduced thickness and small lateral dimensions exhibit high reactivity with oxygen, particularly in the presence of water and accelerated when exposed to light.[10−14] A practical way to address this limitation involves coating the surface of BP flakes obtained by mechanical exfoliation with a thin film of poly(methyl methacrylate) (PMMA) or depositing a layer of aluminum oxide (Al_2O_3) using the atomic layer deposition method.[15,16] In any case, all of the mentioned procedures involve the transfer of BP flakes onto an intermediate target substrate that requires subsequent removal. Additionally, these methods necessitate the use of a glovebox system for both the fabrication and transfer processes.

In practice, along with the size or shape of BP that can be exfoliated, another important issue to address is the effect of the BP size on photothermal efficiency. Fu et al.[17] reported the photothermal properties of BP, showing that large BP flakes exhibited higher photothermal efficiency compared with smaller ones and that large BP flakes were much more effective for the ablation of tumor cells.
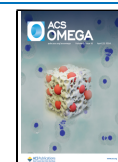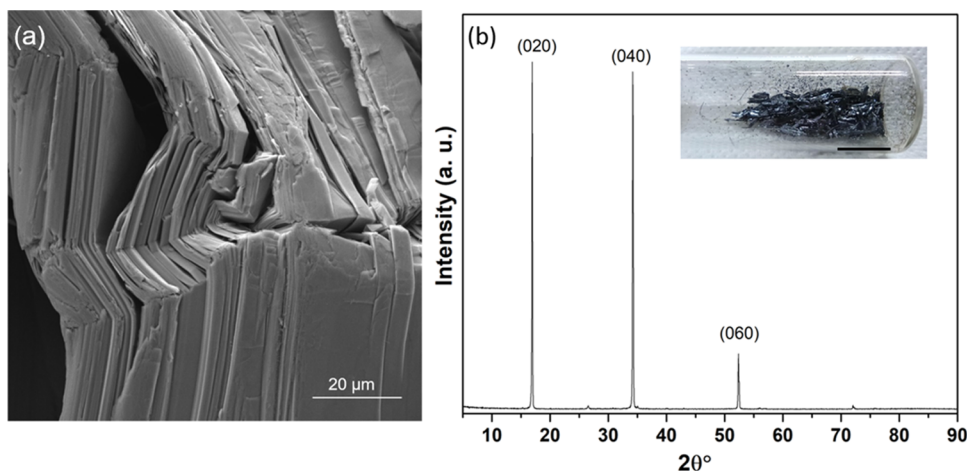
Figure 1. (a) SEM image of synthesized BP crystals. (b) X-ray diffraction (XRD) spectrum of bulk BP powder with the inset showing the photograph of BP crystals; the scale bar indicates 1 cm.

Very recently, it has been reported[18] how van der Waals (vdW) interfaces between two-dimensional (2D) and other substrates promote the transfer of decoupled vdW forces at the interface of interest. This finding, combined with the ability to regulate dispersion through the 2D material—matrix contact area as reported in an elegant experiment by Bilotti et al.,[19] paves the way to use an adhesive matrix to both exfoliate 2D materials and enable control over agglomeration size through the contact area by successive exfoliation steps.

Along with BP, which is an inherent biocompatible inorganic nanomaterial,[20] silk fibroin (SF) is an appealing natural biopolymer for biomedical applications.[21,22] Yang et al.[23] demonstrated the use of SF aqueous solution as an exfoliating agent to produce BP nanosheets with long-term stability and facile solution-processability. Moreover, previous studies indicated that SF films produced from formic acid (FA)/calcium chloride ($CaCl_2$) solutions typically exhibit viscoelastic behavior.[24] Our previous work reported a one-step method to generate an elastomer-like material based only on SF and $CaCl_2$.[25] Furthermore, SF, known for its adhesive properties, has already been studied as an ink for creating printable adhesive patches.[26−29] Given the high viscosity of the SF film (e.g., the glass transition temperature $T_g \approx 170$ °C[29]), we expected that by pressing the film perpendicular to the flat faces of the 2D material, the squeezing flow would produce shear rates large enough to exfoliate the initial multilayered aggregate.[30−32] This method can be viewed as an alternative to the procedure reported in ref 23. This enables the transfer of BP flakes on an SF substrate and subsequent exfoliation in an organic medium, thereby offering multifunctional capabilities for potential biomedical applications. Moreover, SF is an attractive building block that can be three-dimensionally printed from different solutions into various structures for the fabrication of functional composites, as previously shown in refs 26,33.

SF molecules can bind strongly to the BP surface via hydrophobic interactions, and this helps to cover and protect the BP surface from coming in contact with air and humidity; additionally, SF being a polypeptide with hydrophilic tails can improve the dispersibility of BP in water and physiological media, thus preventing its aggregation.[23] Inspired by the Scotch tape method used for graphene, in this study, we combined the advantages of adhesive properties of silk fibroin[34] and the mechanical exfoliation method to develop a "silk fibroin tape" for the fast utilization of high-quality BP, which is storable. Prepared by transferring BP to the surface of an SF carrier film and designing the interfacial adhesion by controlling the SF film composition through simple pressing and peeling off, this silk tape enables uniform BP dispersion on an aqueous solvent. This technique confers stability against oxidation to BP mechanically transferred on SF. In contrast to pristine BP, which rapidly precipitates in a phosphate-buffered saline (PBS) medium,[35] the BP transferred onto SF dissolves in PBS, maintaining the stability of the flakes' dispersion for several days. The biodegradable material based on SF supporting BP exhibited notable photothermal properties, effectively reducing the proliferation of cancer cells in vitro upon exposure to near-infrared radiation. Moreover, SF/BP possesses exceptional processability via extrusion-based printing for the fabrication of micropatterned structures. This feature adds significant value to the SF/BP solution, as 3D printing allows us to precisely and easily define and control the microstructure of the manufactured parts. With high reproducibility, this method allows precise control over the properties of the fabricated structures, encompassing mechanical characteristics and, more broadly, the ability to mimic biological tissues.

This promising SF-assisted exfoliation strategy holds the potential to enhance the utilization of BP nanosheets across a wide range of applications.

■ MATERIALS AND METHODS

Synthesis of BP. High-purity black phosphorus (BP) crystals were synthesized by a small modification of the method reported by Nilges et al.[36,37] All high-purity reactants, red phosphorus (>99.99%), Sn (>99.999%), and SnI_4 (99.999%), used were purchased from Sigma-Aldrich. Red phosphorus, Sn, and catalytic quantities of SnI_4 were placed in a quartz tube of 10 cm in length, with inner and outer diameters of 10 and 13 mm, respectively. The quartz tube was then evacuated and refilled with N_2 gas several times using a vacuum pump and then was sealed under vacuum. It was then heated to 406 °C (with a rate of 4.2 °C/min), kept 2 h at this temperature, and then heated up to 650 °C (with a rate of 2.2 °C/min). The sample was left for 3 days at this temperature in the oven. Afterward, a slow cooling rate was chosen (0.1 °C/

min) to afford the formation of crystals of BP (Figure 1; typical size: 1−2 mm × 3−5 mm). The purity of the synthesized BP crystals was checked by X-ray powder diffraction and scanning electron microscopy (SEM).

Preparation of SF films. Silk cocoons were supplied by a local farm (Fimo srl, Milano, Italy), while $CaCl_2$, FA, and $NaHCO_3$ were supplied by Sigma-Aldrich. Silk cocoons were degummed with $NaHCO_3$ (5 g in 200 mL of water) in boiling water for 30 min and rinsed with deionized water; the procedure was repeated two times. The degummed fibers were then left to dry at room temperature. SF solutions were produced by dispersing the degummed silk fibers into the FA/$CaCl_2$ solution by magnetic stirring at room temperature for 5 min to obtain a homogeneous solution; $CaCl_2$ was in weight ratios (i.e., 80/20 and 60/40) with respect to the silk amount (0.65 g) and it was dissolved in FA (5 mL).[38] SF films were produced by leaving the SF solutions to evaporate onto Petri dishes overnight with subsequent annealing at 40 °C for 2 h to remove any trace of the solvent. SF films were sonicated for 2 h at room temperature in an ultrasonic bath and dissolved in PBS 1×.

Fabrication Protocol. BP neat crystals were glued onto a Scotch tape stick on a flat mica substrate. For the fibroin-assisted exfoliation (FE) process, the SF film was pressed with a force of 50 N so that the SF film could be placed on top of the BP crystal. This step was repeated iteratively, using the SF films as the transferring substrate. The BP flakes transferred to the SF film were weighted and then dissolved in phosphate-buffered saline (PBS; pH 7.4) and sonicated in a bath (40 MHz, 30 °C) for 2 h. For comparison with the neat SF solution, the SF film was dissolved in PBS and sonicated under the same conditions.

Material Characterization. The X-ray diffraction spectrum was recorded on bulk BP crystals with an X'Pert PRO diffractometer (Panalytical), operating in Bragg−Brentano parafocusing geometry with a Cu target and Kα radiation (λ = 1.5418) at 40 kV beam voltage and 40 mA current. The data were collected in the 5−90° 2θ range, with steps of 0.01° and a counting time of 130 s.

Scanning transmission electron microscopy (STEM) experiments were carried out at Ce.ME CNR (Sesto Fiorentino, Italy) using a Dual-Beam TESCAN GAIA3 FIB/SEM ultrahigh resolution field emission microscope at a 10 keV voltage. A piece of BP crystal was placed on the stub, and the results were measured. To investigate the surface morphology, secondary electron images were acquired by using an accelerating voltage of the electron beam of 5 kV.

Raman spectroscopy was performed using a MonoVista CRS S&I spectrometer equipped with a green laser source (532 nm). The laser power was filtered to approximately 5 mW to prevent potential sample photodamage. Point spectra were acquired randomly on the samples' surface using a 10× objective (NA = 0.30) and a 1200 lines/mm grating. An acquisition time of 150 s and a 150 μm slit aperture were used. Measurements were baseline removed and normalized to allow the direct comparison between averaged spectra. Finally, some ratios of interest, namely, A_g^1/A_g^2 and A_g^1/B_{2g} were calculated by integrating the respective peaks' areas.

The surface roughness of few-layer BP after transferring on the SF film was studied using atomic force microscopy (AFM). Contact mode AFM measurements were carried out in air by using a Solver Pro scanning probe microscope (NT-MDT, Moscow, Russia). Rectangular silicon cantilevers, 250 μm long,

having typical spring constants in the range of 0.03−0.2 and 11.5 N/m were used.

The flake dimension analysis was performed by ImageJ on optical images (n = 4) of the SF/BP solution in PBS. Briefly, the region growing segmentation method was used by manually selecting the seeds on the images through the "Set Level" plugin. This allows us to obtain a binary image, where the flasks were set as the objects of interest. Then, the analyze particle tool was used to measure the dimensions of the flasks. Finally, the equivalent diameter of each flask was calculated as in eq 1.

$$ \mathrm{equivalent\,diameter} = \frac{4 \times \mathrm{flask\,area}}{\mathrm{flask\,perimeter}} \tag{1} $$

Rheological data for the SF and SF/BP films were recorded on circular specimens (ca. 12 mm wide and 0.13 mm thick) on an ARES rheometer (Rheometric Scientific). Frequency sweeps were performed at room temperature to find the shear stress of the SF samples with different compositions.

Contact angle measurements of the SF and SF/BP solutions in PBS were performed at room temperature using an optical tensiometer, performing a sessile drop analysis (n = 20, drop volume = 2 μL) according to the Young−Laplace law. Laboratory glass slides, which are a commonly used 3D printing support, were tested as a substrate.

Irradiation and MTT Assay. SF/BP films were sonicated for 2 h at room temperature in an ultrasonic bath and dissolved in PBS 1× in order to get two different BP concentrations: 0.03 and 0.056 mg/mL. The selection of the optimal concentration ratio for photothermal or stabilization effects has been done according to the MTT assay on BP concentrations of 0.3 and 0.56 mg/mL, showing that both concentrations were toxic without and under irradiation (see Figure S4). BP was at the same time dispersed in PBS 1× and sonicated for 2 h with the same condition at 0.056 mg/mL final concentration. MCF7 cells were used as a well-characterized breast cancer cell line and were purchased from Elabscience Biotechnology (Houston, Texas). MCF7 is an adherent, epithelial luminal A cell line positive for the estrogen receptor (ER+) and progesterone receptor (PgR+) and negative for human epidermal growth factor receptor 2 (HER2).[39] Cells were grown in EMEM supplemented with 10% heat-inactivated FBS, 100 IU/mL penicillin/streptomycin, 200 mM L-glutamine, and +1% Non-Energistic Amino Acids (NEAA). Cells were maintained at 37 °C in a saturating humidity atmosphere containing 95% air and 5% CO_2. Cells were seeded 3 × 10^5 in each dish and after 24 h irradiated in air at room temperature with a 300 W xenon light (ThermoOriel solar simulator model 69907). The average powers in a 33 mm diameter output beam in the wavelength range of UVC, UVB, UVA, and visible to near-infrared (Vis−nIR) (400−780 nm) were 11.5, 27, 85, and 430 mW, respectively. The UVC, UVB, and UVA components were shielded by covering the dishes with a polystyrene cap (see Figure S1 in the Supporting Information). The doses of radiation in the Vis−nIR wavelength range during 220 and 440 s exposures were 110 and 220 kJ/m^2, respectively. The photothermal conversion was measured by using a quartz cuvette containing 1 mL of solution, clamped on the top part, and exposed to 300 W xenon light (ThermoOriel solar simulator model 69907). An infrared thermal imaging camera (Fluke Ti27) was used to monitor the temperature change.
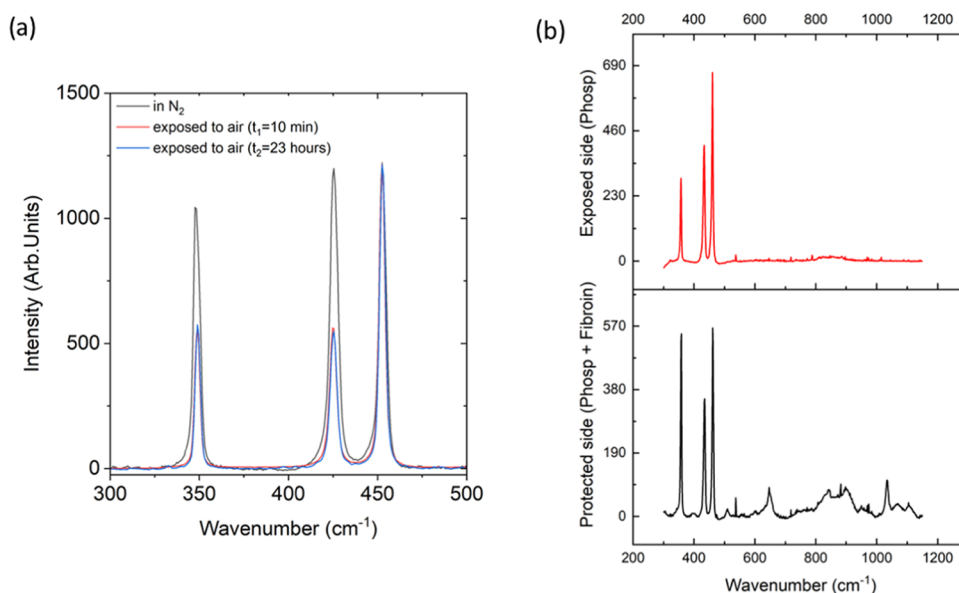
Figure 2. (a) Spectra collected on the BP crystal stored in an N_2 atmosphere to prevent oxidation (black) and after 10 min (red) and 23 h (blue) of air exposure, respectively. (b) Average spectrum of random measurements of the BP crystal collected on the air-exposed (top) and fibroin-exposed (bottom) sides. Characteristic signals of silk fibroin are detected in the spectral region between 600 and 1200 cm^{-1} (bottom).

All treatments (SF, SF/BP final concentrations of 0.03 and 0.056 mg/mL, and BP of 0.056 mg/mL) were performed in PBS 1× to maintain the cells in suitable condition for their life during radiation exposure; in addition, the medium was tapped with a transparent polystyrene cap that was absorbed in the UV optical region. At the same time, cells were treated with SF, SF/BP, and BP alone under the same conditions but without irradiation. After 24 h, the MTT assay was used to test cell viability, as previously reported.[40] MTT reagent was dissolved in PBS 1× and added to each dish at 0.5 mg/mL final concentration. After 3 h of incubation at 37 °C, the supernatant was carefully removed, and formazan salt crystals were dissolved in dimethyl sulfoxide (DMSO, 100 μL) that was added to each well. The absorbance (OD) values were measured spectrophotometrically at 540 nm using a spectrophotometer reader (Jenway 6715 UV/vis, Bibby Scientific Ltd., Dunmow, UK). Each experiment was performed in triplicate, and the results were expressed as a percentage relative to those of the control cells.

Fluorescence Viability Assay by Double Staining with Acridine Orange (AO) and DAPI. The cytotoxicity assessment of SF, SF/BP, and BP (same concentrations tested by the MTT assay and previously reported) was further confirmed by live/dead cells double staining with acridine orange (AO) and DAPI.[41] A NucleoCounter NC-3000 (ChemoMetec A/S, Allerød, Denmark) automated system using fluorescence microscopy and image analysis was used to determine viability (%), live cells (cells/mL), dead cells (cells/mL), total number of cells (cells/mL), and estimated cell diameter (μm) of each condition. Double staining with two fluorescent dyes allows discrimination between live and dead cells. DAPI cannot penetrate the cell membrane; hence, it only stains cells with a permeable cell membrane (i.e., nonviable cells, apoptotic cells) that appear blue. On the contrary, live cells are colored green. The cell suspension (40 μL) together with 10 μL of double staining was loaded in a vial-cassette (ChemoMetec A/S, Allerød, Denmark). The stained cell samples were automatically measured, the fluorescent images were recorded, and a

report showing the results for cell counts and their viability was generated automatically.[42]

3D Printing. Monolayer grid structures were 3D printed on a laboratory slide using a custom-made piston-driven extrusion-based 3D printer.[43,44] The structure gcode was obtained on Slic3r starting from a 1.5 cm × 1.5 cm × 50 μm parallelepiped and applying the following printing parameters: infill = 25%; print speed = 4 mm·s^{-1}; volumetric flow = 0.42 mm^3 s^{-1}; needle diameter = 260 μm. Silk solutions with and without BP were prepared as described above and then sonicated in a bath (40 MHz, 30 °C) for 2 h before printing. The printing occurred at room temperature on a laboratory glass with the printing parameters described above. After the printing process, the structures were dried at room temperature for 24 h; no other postprocessing treatments were required. Then, a morphological analysis of the grids was performed via optical imaging with a bright-field microscope (Leica DM6). Briefly, images of the grid lines were acquired, and their width was measured by using the measurement tool of the microscope software (LASX). Then, a z-stack acquisition was performed (step dimension = 4 μm), and the line profile (i.e., line thickness) was extracted by exploiting Leica Map DCM software.

Statistical Analysis. GraphPad Prism 9.2.0.332 (GraphPad Software, San Diego, CA) was used to assess the statistical significance of all comparison studies in this work. In the statistical analysis for comparison between multiple groups, a two-way analysis of variance (ANOVA) with Tukey's post hoc analysis (multiple comparisons) was conducted with the significance threshold of *$p < 0.05$, **$p < 0.01$, ***$p < 0.001$, and **** $p < 0.0001$.

■ RESULTS AND DISCUSSION

The morphology and structure of as-prepared BP crystals (Figures 1 and 2) were investigated using SEM, XRD, and Raman spectroscopy. Figure 1a shows the appearance of bulk BP flakes after the synthesis. SEM imaging revealed the layered structure of black phosphorus, which is consolidated through
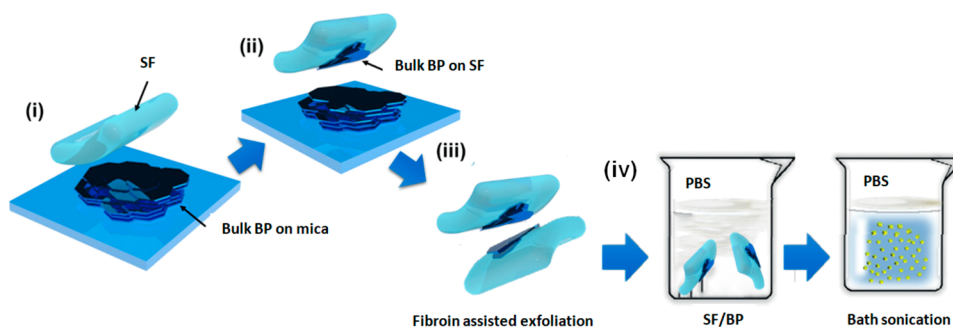
Figure 3. Schematic illustration adapted from ref. 51 of the BP transferring process on the SF substrate and synthesis of SF/BP solution in PBS. (i) Mechanical exfoliation of BP flakes from bulk BP using viscoelastic SF, (ii) pick-up process of exfoliated BP flakes from the scotch tape, (iii) iterative silk fibroin-assisted exfoliation on another SF substrate, and (iv) dissolution and exfoliation of SF/BP in an ultrasonic bath.

weak van der Waals forces, facilitating its sequential peeling off layer by layer (Figure 1a).

The X-ray diffraction spectrum of synthesized BP powder features the typical pattern of elemental black phosphorus[45] having an orthorhombic crystal structure, with three intense peaks at $2\theta° = 16.9, 34.2,$ and $52.3°$ corresponding to the (020), (040), and (060) planes of BP, respectively, as shown in Figure 1b. This confirms the high crystallinity and purity of the in-house-produced black phosphorus.

The Raman spectrum of bulk BP (Figure 2a) shows the characteristic A_g^1, B_{2g}, and A_g^2 vibrations.[46] The relative intensities of these three bands can serve to monitor both the oxidation state and the results of exfoliation of as-prepared BP crystals.[47] Indeed, a comparative analysis between spectra recorded on the surface of the BP crystals under two different environmental conditions reveals that in a N_2 atmosphere (Figure 2a black spectrum), the ratio of A_g^1 to A_g^2 intensities is approximately equal to 1. However, exposure to oxygen leads to a reduction in this ratio, as shown in the red spectrum in Figure 2a. This is related to the modification of the BP crystal surface, probably due to the oxidation of phosphorus atoms on its surface,[48−50] which occurs very rapidly (only 10 min) and remains constant over time (Figure 2a blue spectrum). The protective effect of silk fibroin was verified by recording the spectra of BP flakes on both the side exposed to air and the one covered by the film (Figure 3). The results clearly reveal that the surface of the BP crystals exposed to air (Figure 2b, top) underwent an oxidation process, while the one protected by the SF film (Figure 2b, bottom) was preserved, as shown by the ratio between the A_g^1 and A_g^2 intensities.

The SF film treatment was then used to mechanically exfoliate the bulk BP crystal due to its rheological properties (Figure 3).

Figure 4 shows the shear stresses of the SF films at 25 °C. Conformal transitions of the secondary structure of SF films and thus mechanical properties can be tuned by adjusting the calcium ion content. This is because calcium ions can capture water molecules from the atmosphere and change the coordination with the SF protein;[38] for this motivation, two different films obtained by changing the $SF/CaCl_2$ ratio were tested (e.g., 80/20 and 60/40).[38] Given the high viscosity of the SF (we are working just above the glass transition temperature),[29] fitting the SF data using the power law for the viscous stress (τ) as a function of the shear rate (dγ/dt), $\tau \simeq \kappa(d\gamma/dt)^n$, we obtain $\kappa \approx 10$ and 2 (in SI units) and $n \approx 1.7$ and 2.82 for the 80:20 and 60:40 SF compositions, respectively. Assuming a uniform biaxial extensional flow, the
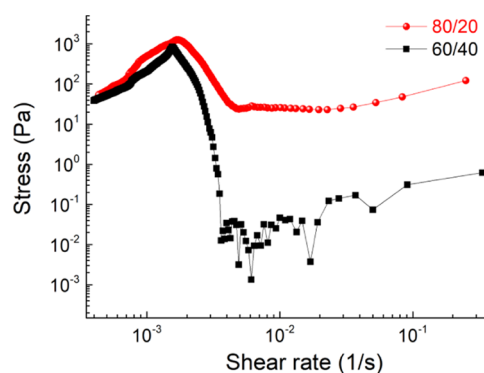

Figure 4. Shear stresses as a function of shear rates of 60/40 and 80/20 SF compositions. Measurements were taken with samples at 25 °C.

shear rate can also be written as dγ/dt $= \sqrt{3}(dh/dt)/h$,[19,31] where in our experiment, we assume dh/dt $\simeq$1.8 mm/s and h varies from 4 to 0.5 mm. During the compression, these data restitute dγ/dt values between ∼0.8 and ∼6 s^{-1} as values representative of the initial and final thickness change due to compression, respectively. Using these reference values, the corresponding viscous stresses are estimated to be between 34 Pa (for the 60/40 composition) and 134 kPa (for the 80/20 composition). These shear stresses are sufficient to exfoliate the initial BP crystals with the surface energy of BP $\Gamma \cong 80$ mN/m,[49] which for a flake diameter of the BP crystal of 4.3 mm gives a value of ∼18 Pa. Herein, the 80/20 composition has been used for the transfer process.

The successful mechanical transfer and exfoliation of BP onto the SF films were confirmed by Raman spectroscopy (Figure 5a). Specifically, the Raman data in Figure 5a report the average spectra collected on the air-exposed side of BP crystals mechanically exfoliated by SF films in successive transferring cycles (FE1 to FE3), confirming a decrease in the A_g^1/A_g^2 ratio due to BP oxidation with respect to nonexposed crystals. Furthermore, the relative ratio R between the A_g^1 and B_{2g} intensities was used to monitor the reduction of the BP flake thickness due to the exfoliation process.[50] The distribution of R values, shown in the box plot of Figure 5b, exhibits a progressive decrease going from the bulk material ($R_{BULK} = 1.18$) to the fibroin silk-exfoliated flakes and going from the first to the last exfoliation cycle ($R_{FE1} = 0.73$; $R_{FE2} = 0.58$; $R_{FE3} = 0.55$). To correlate the spectroscopic information on transferred BP flakes, we measured the thickness of a sample of BP on SF by AFM and STEM before and after the exfoliation process (Figures S2 and 5c). According to what was
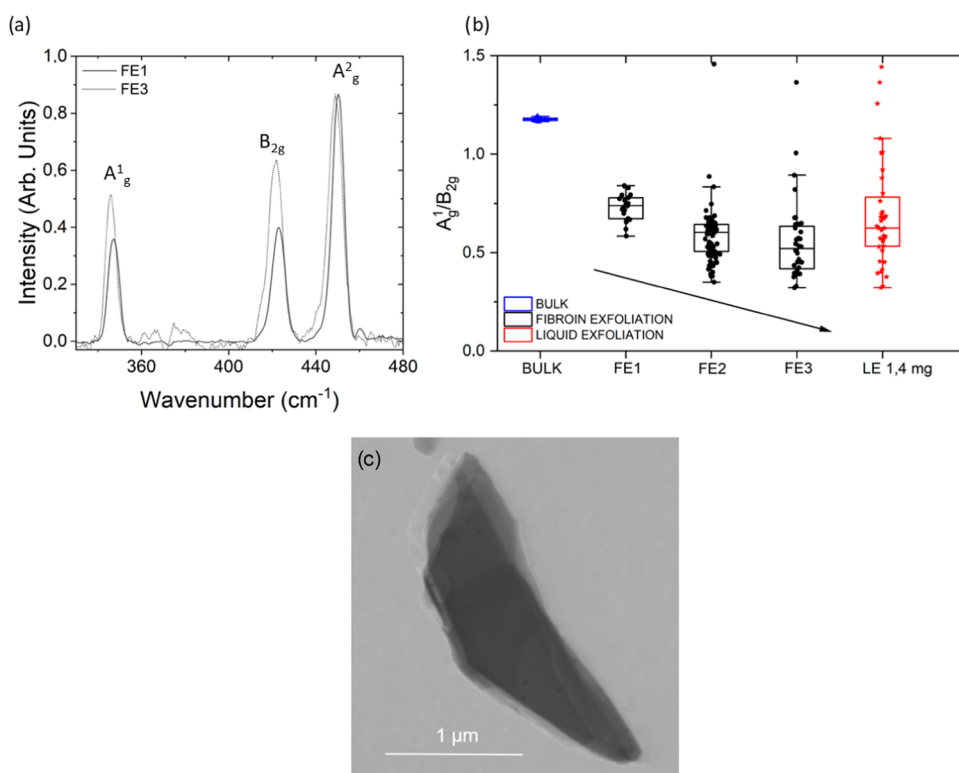
Figure 5. (a) Averaged spectra of random measurements collected on the air-exposed side of BP crystals after consecutive cycles of silk fibroin exfoliation. (b) Box plots of the ratio between the intensities of the A_g^1 and B_{2g} peaks of random spectra collected on the air-exposed side of bulk BP (blue dots), BP subjected to successive cycles of mechanical exfoliation (FE1−FE2−FE3, black), and BP subjected to liquid exfoliation. (c) STEM bright-field image of the BP flake obtained after the FE3 exfoliation process from 80/20 SF in formic acid.

reported by Coleman et al.,[50] we can observe a correlation of relative A_g^1/B_{2g} band intensities to varying thicknesses. To show the advantages of the exfoliation method such as the SF-mediated BP yield, as shown in Figure 5c, the STEM bright-field image of the BP flake obtained after the FE3 exfoliation process from 80/20 SF was reported. From the flake edge, seven layers can be counted, and considering an interlayer spacing of 0.53 nm (e.g., 6 × 0.53 nm 3.18 nm) plus the thickness of each layer (e.g., 0.22 nm, the distance P−P, 0.22 × 7 = 1.54 nm), a total thickness of 4.72 nm was obtained after FE3. Our data show that R increases with increasing the number of layers. Finally, the same ratio was measured for BP flakes obtained by liquid exfoliation of SF/PB in PBS, giving a value of about $R_{LE} = 0.68$, intermediate between the ones obtained after one and two cycles of fibroin mechanical exfoliation.

To evaluate the influence of SF on the stability of BP, the BP and SF/BP flakes were dispersed in PBS 1× and examined at 0, 10 min, 20 min, and 1 day. As shown in Figure 6a, the color of the solution containing the bare BP becomes clear after 1 day, while the SF/BP solutions retain an opaque color with respect to the SF solution. As shown in Figure 6b, by sonicating at room temperature for 2 h, a sample of bulk BP dispersed in PBS, very thick BP flakes are obtained in solution. On the other hand, when a dispersion of SF/BP in PBS is sonicated for the same time, much thinner BP flakes are detected, as evidenced by Figure 6c. A panoramic view of this sample is reported in Figure 6d with an inset of size distribution, showing that the lateral dimension of the BP flakes is in the range of 3−7 μm. Going to a higher magnification, it is possible to count the number of superimposed layers, as shown

in Figure 6d right, that being five layers, accounting for a thickness of 2.5 nm, considering an interlayer spacing of 0.53 nm as known from the literature and a thickness of around 0.22 nm for each layer, sum up 3.32 nm.[50] This finding can be rationalized in terms of the higher viscosity of SF solution that exerts a higher shear stress, leading to a more uniform dispersion of BP flakes. The photothermal performance of the SF/BP in PBS is reported in Figure 6e. After 1 min of irradiation with 50 W cm^{-2}, the temperature of the SF/BP solution increases by 10 °C, while the SF solution reaches the temperature of the SF/BP solution after 4 min. The intrinsic absorbances in the UV and nIR bands of SF (see Figure S3 in the Supporting Information) decreased slightly the photothermal properties of the SF/BP solution with respect to those of BP, while acting synergistically results in an increase of the temperature of the SF/BP solution after 1 min.

Based on these findings and previous studies that reported the property of BP to convert near-infrared light into thermal energy,[23] we performed an in vitro experiment on MCF7 cancer cell proliferation through Vis−nIR irradiation by using SF, BP, and SF/BP as media for cell growth (Figure 7). The in vitro cytotoxicity assay of the SF, SF/BP, and BP media toward tumor cells is reported in Figure 7a. The viability of the MCF7 cells, incubated with the different media, indicates no significant cytotoxicity without irradiation (in gray). After irradiation of 220 s (in blue), the viability decreased by more than 20% with 0.03 mg of SF/BP and about 30% with 0.056 mg of SF/BP and 0.056 mg of BP alone. A significant decrease in cell viability was observed in the presence of BP when the cells were incubated for a longer period of 440 s (in orange). The photothermal ability of SF/BP and BP to kill cancer cells
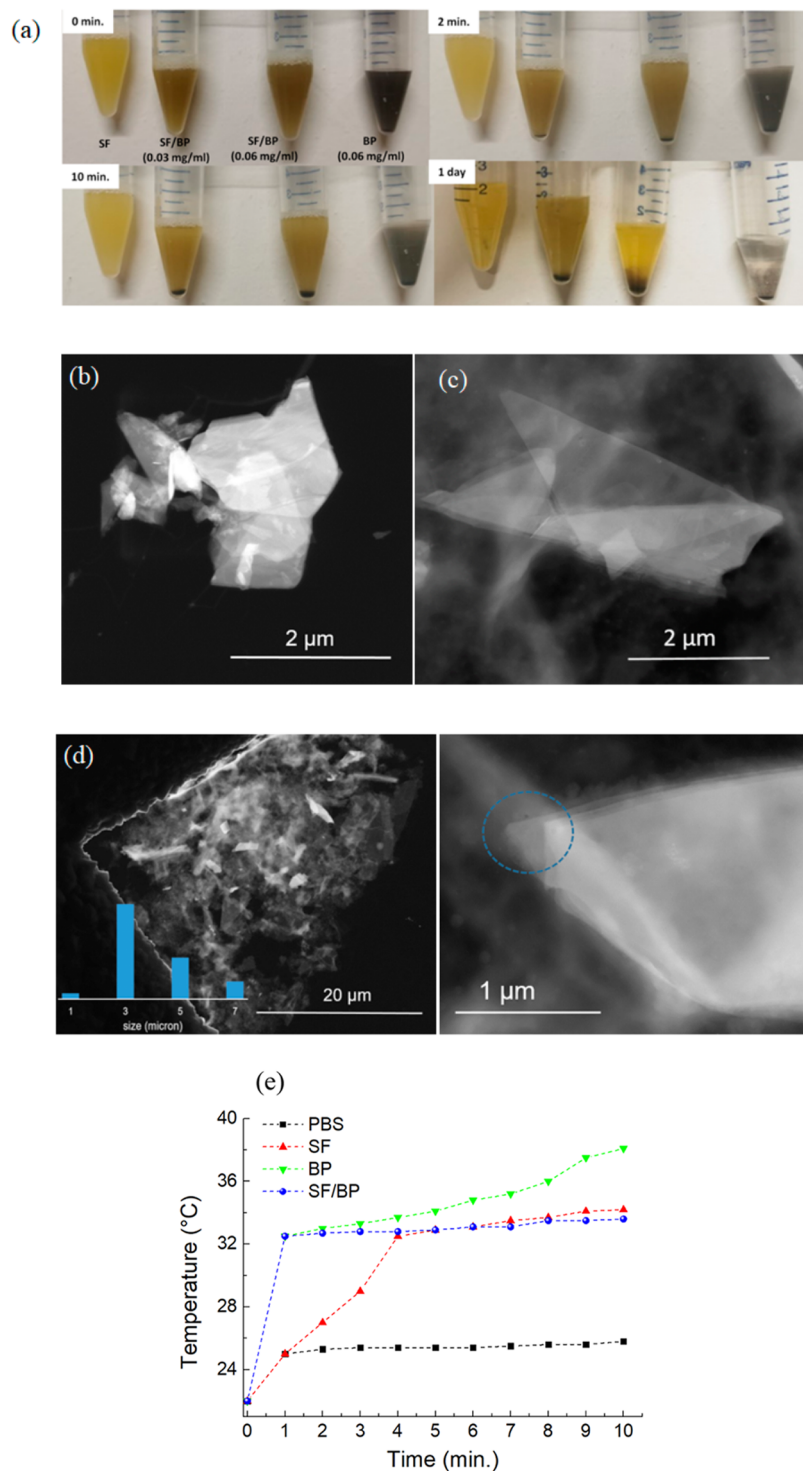
Figure 6. (a) Photographs of SF, SF/BP, and BP after storage in PBS for different periods of time. Dark-field STEM images of (b) BP dispersed in PBS and (c) SF/BP dispersed in PBS. (d) STEM dark-field image of SF/BP in PBS. Left: panoramic view with the inset showing the relative size distribution; right: edges of a selected BP flake, showing the superimposition of layers. (e) Photothermal heating curves of BP, SF, and SF/BP after dissolving in PBS for 2 h and being irradiated with 50 W cm^{-2} for 10 min. The heating curve of neat PBS is also reported as a reference.

is then investigated. A dose-dependent photothermal effect of the BP flakes can be observed. Almost 50% of the cancer cells are killed after incubation with BP and exposure to a dose of 440 s of Vis−nIR irradiation. On the contrary, the same treatment in the presence of SF/BP instead of BP does compromise 25% cell viability.

These results were confirmed with a fluorescence viability assay by double staining with acridine orange (AO) and DAPI (Figure 7b). The CTR cells (in PBS 1×) exhibited a 90.6% viability that remains approximately unchanged after 220 s (86.2%) and 440 s (83.2%) of irradiation. The estimated cell diameter for CTR cells was around 19 μm (as reported in Table S1). On the contrary, 0.03 mg of SF/BP, 0.056 mg of
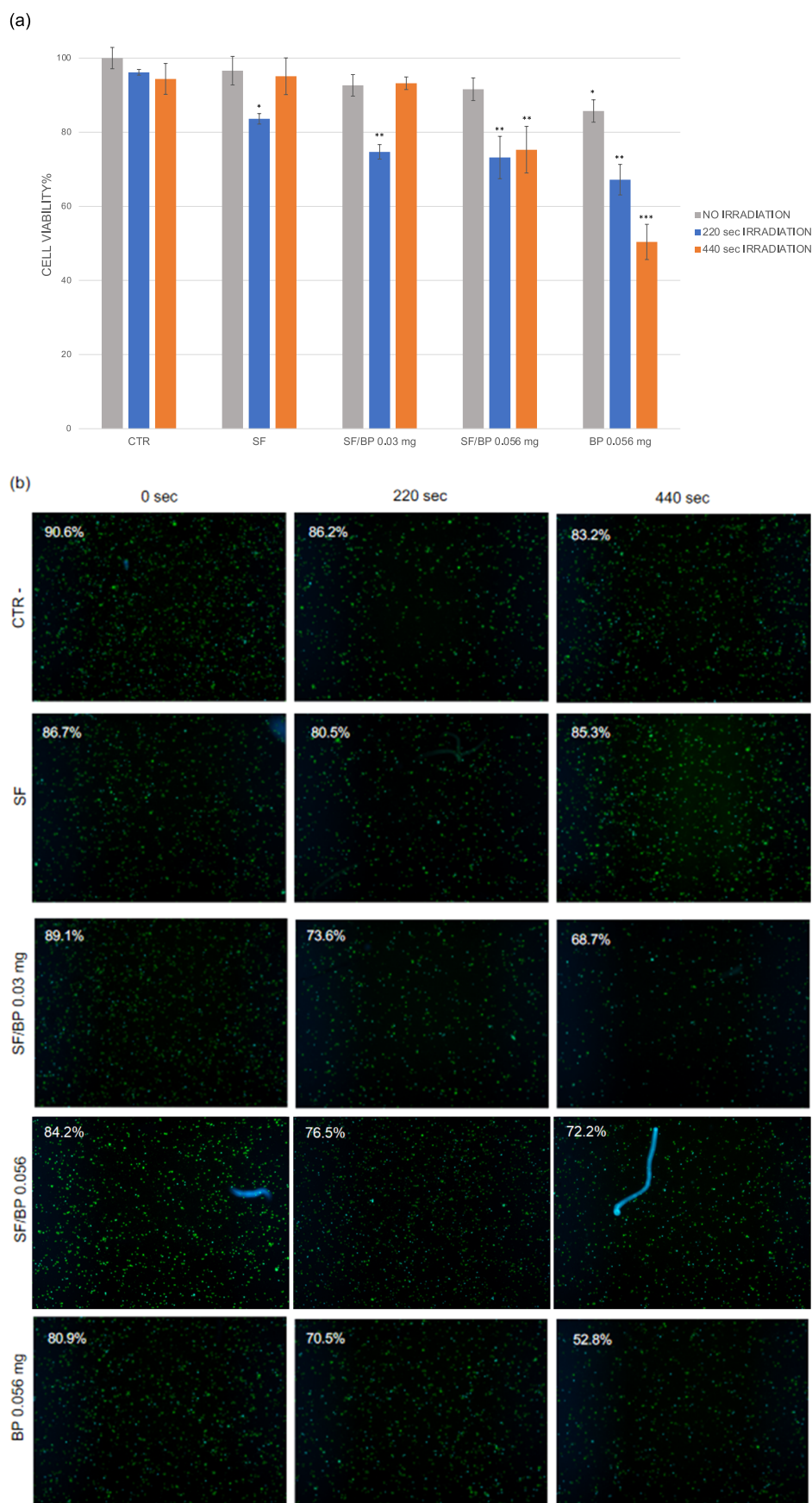
(a)

(b)

Figure 7. (a) Viability of MCF7 cancer cells after 24 h of incubation with PBS 1× (CTR), SF, SF/BP 0.03 mg, SF/BP 0.056 mg, and BP 0.056 mg reported without irradiation (in gray), irradiation with a 110 kJ/m^2 dose for 220 s (in blue), and irradiation with a 220 kJ/m^2 dose for 440 s (in orange). (b) AO−DAPI double staining was performed for each condition, and viability (%) was reported in each image.
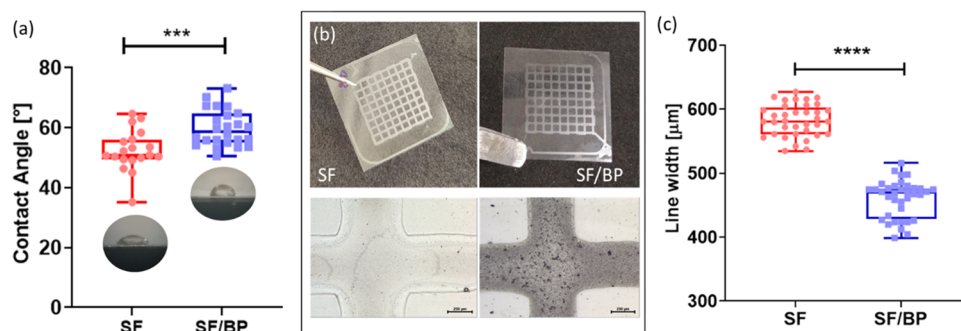
Figure 8. (a) Contact angle measurements (deg) performed on laboratory slides. (b) Optical image of the monolayer grids fabricated via extrusion-based 3D printing and a zoom-in image of the grid lines and intersection (scale bar = 250 μm). (c) Line width [μm] measurements of the printed grids.

SF/BP, and 0.056 mg of BP treatments were able to decrease cell viability, and in part, this effect was evident also in the cell diameter that became lower (Table S1). In particular, 0.056 mg of BP alone after 440 s led to 52.8% cell viability, meaning that the number of live and dead cells was approximately the same and the cell diameter was around 17.1 μm (see Table S1).

In this study, we aimed to fabricate 2D micropatterned grids. The accuracy of the printing process depends on four main parameters: the stand-off distance, printing speed, substrate surface property, and material viscosity.[52,53] Both the stand-off distance and the printing speed are not related to the involved inks but depend on the 3D printer. Regarding the latter parameters, since in this study, the viscosity is low (in the order of cPa*s, data not shown),[54] the surface energy of the printing substrate is the most relevant property to infer the printed line retention, as described by the dimensionless Ohnesorge number.[55] Moreover, since the desired structures do not evolve in the 3D space, nor have protrusion planes or hanging parts, the rheological properties (i.e., shear thinning behavior, high yield stress, and high viscosity at rest[56,57]) do not come into play and, therefore, were not investigated as printability indicators. Instead, contact angle measurements were performed to reveal the wettability of the laboratory slide (namely, the printing substrate) by the SF and SF/BP solutions. The decrease in the wettability of the printing substrate, associated with a high contact angle, can be related to a decrease in the printed line diameter and therefore to a better printing accuracy. This is because when the wettability increases, the spreading of the deposited line increases as well, thus leading to a decrease in the printing accuracy. As a consequence, on the one hand, low wettability could be beneficial for printing accuracy. However, on the other hand, extremely low wettability could lead to the pinch off of the deposited line and consequently to the creation of separate drops (Plateau−Rayleigh instability). This will entail a completely negative outcome of the printing process. Thus, the surface tension should be high enough to guarantee a confined line but not excessively high enough to lead to the Plateau−Rayleigh instability. This value has been reported in the literature to be around 90°.[58] As can be seen from Figure 8a, the contact angle increased when the SF/BP solution was tested ($p > 0.001$), thus ensuring better line retention for the BP-enriched SF solution. As can be seen from Figure 8b, the printing tests were favorable, leading to the fabrication of monolayer grids on laboratory slides. Morphological analysis of the grids revealed a statistically significant difference in the line

width dimension among the two solutions, with a higher line retention when BP is added to the SF solution, in accordance with contact angle measurements (Figure 8a−c). Finally, the line profiles were extracted from the z-stacks. This allows us to evaluate the thickness of the lines (Figures S5 and S6), which is approximately equal to 100 μm for the SF solution and 70 μm for the SF/BP solution. This difference can be due to the different concentrations of the involved solutions. The line width and the line thickness could be used together in the future to design more complex structures that can be fabricated through extrusion-based 3D printing.

CONCLUSIONS

In this study, we developed a silk tape that acted as an exfoliating agent, enhancing the storability of BP flakes. The silk tape was soluble in an aqueous environment, increasing the BP stability in the physiological medium without any cell toxicity effects. In the framework of designing a light-responsive biomaterial, in vitro cancer cell viability experiments demonstrate the tumor ablation efficiency under NIR radiation when BP flakes interact with the SF multidomain structure in a PBS medium. We finally reported the processability of such materials via extrusion-based printing for the fabrication of micropatterned structures. In perspective, the development of a novel silk tape for the storage and fast utilization of 2D nanomaterials with good biocompatibility and light absorption properties can find many applications in the medical field.

ASSOCIATED CONTENT

Ⓢ Supporting Information

The Supporting Information is available free of charge at https://pubs.acs.org/doi/10.1021/acsomega.3c09461.

> UV−vis absorption spectrum of PS cap (Figure S1); representative atomic force microscopic (AFM) images showing the topography of bulk BP flakes glued on the mica substrate before and after the first mechanical exfoliation (Figure S2); ATR-FTIR spectra of SF and SF/BP films (Figure S3); viability of MCF7 cancer cells and the AO−DAPI double staining experiment (Figure S4); line profile extraction of the SF solution performed by Leica Map CDM Software (Figure S5); line profile extraction of the SF/BP solution performed by Leica Map CDM Software (Figure S6); and viability, live cells, dead cells, total number of cells, and estimated cell diameter from the Acridine Orange−DAPI double staining assay (Table S1) (PDF)

■ AUTHOR INFORMATION

Corresponding Author

Luca Valentini − *Civil and Environmental Engineering Department and INSTM Research Unit, University of Perugia, 05100 Terni, Italy;* ⊙ orcid.org/0000-0002-6803-5889; Email: luca.valentini@unipg.it

Authors

Martina Alunni Cardinali − *Department of Chemistry, Biology and Biotechnology, University of Perugia, 06123 Perugia, Italy*

Maria Rachele Ceccarini − *Department of Pharmaceutical Science, University of Perugia, 06123 Perugia, Italy*

Irene Chiesa − *Department of Ingegneria dell'Informazione and Research Center E. Piaggio, University of Pisa, Pisa 56122, Italy;* ⊙ orcid.org/0000-0002-1260-4990

Silvia Bittolo Bon − *Dipartimento di Fisica e Geologia, Università degli Studi di Perugia, 06123 Perugia, Italy;* ⊙ orcid.org/0000-0002-1546-5826

Tommaso Rondini − *Department of Pharmaceutical Science, University of Perugia, 06123 Perugia, Italy*

Manuel Serrano-Ruiz − *Institute of Chemistry of OrganoMetallic Compounds-ICCOM, National Research Council-CNR, 50019 Sesto Fiorentino, Italy;* ⊙ orcid.org/0000-0002-6372-3586

Maria Caporali − *Institute of Chemistry of OrganoMetallic Compounds-ICCOM, National Research Council-CNR, 50019 Sesto Fiorentino, Italy;* ⊙ orcid.org/0000-0001-6994-7313

Silvia Tacchi − *CNR-IOM − Istituto Officina dei Materiali, National Research Council of Italy, 06123 Perugia, Italy*

Alberto Verdini − *CNR-IOM − Istituto Officina dei Materiali, National Research Council of Italy, 06123 Perugia, Italy;* ⊙ orcid.org/0000-0001-8880-2080

Caterina Petrillo − *Dipartimento di Fisica e Geologia, Università degli Studi di Perugia, 06123 Perugia, Italy*

Carmelo De Maria − *Department of Ingegneria dell'Informazione and Research Center E. Piaggio, University of Pisa, Pisa 56122, Italy;* ⊙ orcid.org/0000-0002-1368-3571

Tommaso Beccari − *Department of Pharmaceutical Science, University of Perugia, 06123 Perugia, Italy*

Paola Sassi − *Department of Chemistry, Biology and Biotechnology, University of Perugia, 06123 Perugia, Italy;* ⊙ orcid.org/0000-0002-4920-2784

Complete contact information is available at:
https://pubs.acs.org/10.1021/acsomega.3c09461

Author Contributions

The manuscript was written with the contributions of all authors. All authors have approved the final version of the manuscript. M.A.C., M.R.C., I.C., S.B.B., M.S.-R., and S.T. were involved in laboratory research. M.A.C., M.R.C., I.C., C.D.M., M.C., P.S., and L.V. wrote the original draft. All of the authors revised the original draft. L.V., P.S., and C.D.M. contributed to the conceptualization of experiments and L.V. contributed to the overall coordination of the research activities. All authors have read and agreed to the published version of the manuscript.

■ REFERENCES

(1) Takao, Y.; Morita, A. Electronic structure of black phosphorus: tight binding approach. *Physica B+C* **1981**, *105*, 93−98.

(2) Wang, Y.; Wu, F.; Liu, X.; Lin, J.; Chen, J.-Y.; Wu, W.-W.; Wei, J.; Liu, Y.; Liu, Q.; Liao, L. High on/off ratio black phosphorus based memristor with ultra-thin phosphorus oxide layer. *Appl. Phys. Lett.* **2019**, *115*, No. 193503.

(3) Zhong, J.-H.; Zhou, Y.; Tian, X.-X.; Sun, Y.-L.; Shi, B.-R.; Zhang, Z.-Y.; Zhang, W.-H.; Liu, X.-D.; Yang, Y.-M. The addition of an ultra-small amount of black phosphorous quantum dots endow self-healing polyurethane with a biomimetic intelligent response. *Macromol. Rapid Commun.* **2023**, *44*, No. 2300286.

(4) Qu, G.; Xia, T.; Zhou, W.; Zhang, X.; Zhang, H.; Hu, L.; Shi, J.; Yu, X. F.; Jiang, G. Property-activity relationship of black phosphorus at the nano-bio interface: from molecules to organisms. *Chem. Rev.* **2020**, *120*, 2288−2346.

(5) Yang, X.; Wang, D.; Zhu, J.; Xue, L.; Ou, C.; Wang, W.; Lu, M.; Song, X.; Dong, X. Functional black phosphorus nanosheets for mitochondria- targeting photothermal/photodynamic synergistic cancer therapy. *Chem. Sci.* **2019**, *10*, 3779−3785.

(6) Liu, W.; Dong, A.; Wang, B.; Zhang, H. Current advances in black phosphorus-based drug delivery systems for cancer therapy. *Adv. Sci.* **2021**, *8*, No. 2003033.

(7) He, J.; Chen, G.; Zhao, P.; Ou, C. Near-infrared light-controllable bufalin delivery from a black phosphorus-hybrid supramolecular hydrogel for synergistic photothermal-chemo tumor therapy. *Nano Res.* **2021**, *14*, 3988−3998.

(8) Tang, Z.; Kong, N.; Ouyang, J.; Feng, C.; Kim, N. Y.; Ji, X.; Wang, C.; Farokhzad, O. C.; Zhang, H.; Tao, W. Phosphorus Science-oriented designand synthesis of multifunctional nanomaterials for biomedical applications. *Matter* **2020**, *2*, 297−322.

(9) Kang, Y.; Li, Z.; Lu, F.; Su, Z.; Ji, X.; Zhang, S. Synthesis of red/black phosphorus-based composite nanosheets with a Z-scheme heterostructure for high-performance cancer phototherapy. *Nanoscale* **2022**, *14*, 766−779.

(10) Wang, H.; Yang, X.; Shao, W.; Chen, S.; Xie, J.; Zhang, X.; Wang, J.; Xie, Y. Ultrathin black phosphorus nanosheets for efficient singlet oxygen generation. *J. Am. Chem. Soc.* **2015**, *137*, 11376−11382.

(11) Sun, Z.; Xie, H.; Tang, S.; Yu, X.-F.; Guo, Z.; Shao, J.; Zhang, H.; Huang, H.; Wang, H.; Chu, P. K. Ultrasmall black phosphorus quantum dots: synthesis and use as photothermal agents. *Angew. Chem.* **2015**, *127*, 11688−11692.

(12) Island, J. O.; Steele, G. A.; Van der Zant, H. S.; Castellanos-Gomez, A. Environmental instability of few-layer black phosphorus. *2D Mater.* **2015**, *2*, No. 011002.

(13) Huang, Y.; Qiao, J.; He, K.; Bliznakov, S.; Sutter, E.; Chen, X.; Luo, D.; Meng, F.; Su, D.; Decker, J.; Ji, W.; Ruoff, R. S.; Sutter, P. Interaction of black phosphorus with oxygen and water. *Chem. Mater.* **2016**, *28*, 8330−8339.

(14) Wang, G.; Slough, W. J.; Pandey, R.; Karna, S. P. Theoretical study of stability of phosphorene in air. *2D Mater.* **2016**, *3* (2), No. 025011.

(15) Alsaffar, F.; Alodan, S.; Alrasheed, A.; Alhussain, A.; Alrubaiq, N.; Abbas, A.; Amer, M. R. Raman sensitive degradation and etching dynamics of exfoliated black phosphorus. *Sci. Rep.* **2017**, *7*, No. 44540.

(16) Na, J.; Lee, Y. T.; Lim, J. A.; Hwang, D. K.; Kim, G.; Choi, W. K.; Song, Y. Few-layer black phosphorus field-effect transistors with reduced current fluctuation. *ACS Nano* **2014**, *8*, 11753−11762.

(17) Fu, H.; Li, Z.; Xie, H.; Sun, Z.; Wang, B.; Huang, H.; Han, G.; Wang, H.; Chu, P.; Yu, X. Different-sized black phosphorus nanosheets with good cytocompatibility and high photothermal performance. *RSC Adv.* **2017**, *7*, 14618.

(18) Satterthwaite, P. F.; Zhu, W.; Jastrzebska-Perfect, P.; Tang, M.; Spector, S. O.; Gao, H.; Gao, H.; Kitadai, H.; Kitadai, H.; Lu, A.-Y.; Lu, A. Y.; Tan, Q.; Tang, S.-Y.; Tang, S. Y.; Chue, Y.-L.; Chueh, Y. L.; Kuo, C.-N.; Kuo, C. N.; Shan Lue, C.; Lue, C. S.; Kong, J.; Kong, J.; Ling, X.; Ling, X.; Niroui, F. Van der Waals device integration beyond the limits of van der Waals forces using adhesive matrix transfer. *Nat. Electron.* **2024**, *7*, 17−28, DOI: 10.1038/s41928-023-01079-8.

(19) Santagiuliana, G.; Picot, O. T.; Crespo, M.; Porwal, H.; Zhang, H.; Li, Y.; Rubini, L.; Colonna, S.; Fina, A.; Barbieri, E.; Spoelstra, E. B.; Mirabello, G.; Patterson, J.; Botto, L.; Pugno, N. M.; Peijs, T.; Bilotti, E. Breaking the nanoparticle loading − dispersion dichotomy in polymer nanocomposites with the art of croissant-making. *ACS Nano* **2018**, *12*, 9040−9050.

(20) Childers, D. L.; Corman, J.; Edwards, M.; Elser, J. J. Sustainability challenges of phosphorus and food: solutions from closing the human phosphorus cycle. *BioScience* **2011**, *61*, 117−124.

(21) Pravst, I. Risking public health by approving some health claims? − The case of phosphorus. *Food Policy* **2011**, *36*, 726−728.

(22) Farokhi, M.; Mottaghitalab, F.; Samani, S.; Shokrgozar, M. A.; Kundu, S. C.; Reis, R. L.; Fatahi, Y.; Kaplan, D. L. Silk fibroin/hydroxyapatite composites for bone tissue engineering. *Biotechnol. Adv.* **2018**, *36* (1), 68−91.

(23) Huang, X.-W.; Wei, J.-J.; Zhang, M.-Y.; Zhang, X.-L.; Yin, X.-F.; Lu, C. H.; Song, J.-B.; Bai, S.-M.; Yang, H.-H. Water-based black phosphorus hybrid nanosheets as a moldable platform for wound healing applications. *ACS Appl. Mater. Interfaces* **2018**, *10*, 35495−35502.

(24) Valentini, L.; Ceccarini, M. R.; Verdejo, R.; Tondi, G.; Beccari, T. Stretchable, bio-compatible, antioxidant and self-powering adhesives from soluble silk fibroin and vegetal polyphenols exfoliated graphite. *Nanomaterials* **2021**, *11*, 2352.

(25) Bon, S. B.; Chiesa, I.; Degli Esposti, M.; Morselli, D.; Fabbri, P.; De Maria, C.; Morabito, A.; Coletta, R.; Calamai, M.; Pavone, F. S.; Tonin, R.; Morrone, A.; Giorgi, G.; Valentini, L. Carbon nanotubes/regenerated silk composite as a three-dimensional printable bio-adhesive ink with self-powering properties. *ACS Appl. Mater. Interfaces* **2021**, *13*, 21007−21017.

(26) Zou, Y.-P.; Liang, H.-F.; Wang, B.; Zhang, Q.-C.; Su, D.-H.; Lu, S.-Y.; Zhang, Q.-Y.; Wu, T.; Xiao, L.; Xiao, Y.; Dong, J.; et al. Precipitation-based silk fibroin fast gelling, highly adhesive, and magnetic nanocomposite hydrogel for repair of irregular bone defects. *Adv. Funct. Mater.* **2023**, *33*, No. 2302442.

(27) Jiang, K.; Wu, Q.; Chen, Y.; Fan, D.; Chu, F. A high-performance bio-based adhesive comprising soybean meal, silk fibroin, and tannic acid inspired by marine organisms. *Int. J. Biol. Macromol.* **2023**, *242*, No. 125095.

(28) Bai, S.; Zhang, X.; Cai, P.; Huang, X.; Huang, Y.; Liu, R.; Zhang, M.; Song, J.; Chen, X.; Yang, H. A silk-based sealant with tough adhesion for instant hemostasis of bleeding tissues. *Nanoscale Horiz.* **2019**, *4*, 1333−1341.

(29) Nakamura, S.; Saegusa, Y.; Yamaguchi, Y.; Magoshi, J.; Kamiyama, S. Physical properties and structure of silk. XI. Glass transition temperature of wild silk fibroins. *J. Appl. Polym. Sci.* **1986**, *31*, 955−956.

(30) Leider, P. J.; Bird, R. B. Squeezing flow between parallel disks. I. Theoretical analysis. *Ind. Eng. Chem. Fundam.* **1974**, *13*, 336−341.

(31) Engmann, J.; Servais, C.; Burbidge, A. S. Squeeze flow theory and applications to rheometry: a review. *J. Non-Newtonian Fluid Mech.* **2005**, *132*, 1−27.

(32) Barwich, S.; Coleman, J. N.; Möbius, M. E. Yielding and flow of highly concentrated, few-layer graphene suspensions. *Soft Matter* **2015**, *11*, 3159−3164.

(33) Ceccarini, M. R.; Palazzi, V.; Salvati, R.; Chiesa, I.; De Maria, C.; Bonafoni, S.; Mezzanotte, P.; Codini, M.; Pacini, L.; Errante, F.; Rovero, P.; Morabito, A.; Beccari, T.; Roselli, L.; Valentini, L. Biomaterial inks from peptide-functionalized silk fibers for 3D printing of futuristic wound-healing and sensing materials. *Int. J. Mol. Sci.* **2023**, *24*, 947.

(34) Chiesa, I.; De Maria, C.; Ceccarini, M. R.; Mussolin, L.; Coletta, R.; Morabito, A.; Tonin, R.; Calamai, M.; Morrone, A.; Beccari, T.; Valentini, L. 3D printing silk-based bioresorbable piezoelectric self-adhesive holey structures for in vivo monitoring on soft tissues. *ACS Appl. Mater. Interfaces* **2022**, *14*, 19253.

(35) Sun, Z.; Xie, H.; Tang, S.; Yu, X. F.; Guo, Z.; Shao, J.; Zhang, H.; Huang, H.; Wang, H.; Chu, P. K. Ultrasmall black phosphorus quantum dots: synthesis and use as photothermal agents. *Angew. Chem., Int. Ed.* **2015**, *54*, 11526−11530.

(36) Nilges, T.; Kersting, M.; Pfeifer, T. A fast low-pressure transport route to large black phosphorus single crystals. *J. Solid State Chem.* **2008**, *181*, 1707−1711.

(37) Köpf, M.; Eckstein, N.; Pfister, D.; Grotz, C.; Krüger, I.; Greiwe, M.; Hansen, T.; Kohlmann, H.; Nilges, T. Access and in situ growth of phosphorene-precursor black phosphorus. *J. Cryst. Growth* **2014**, *405*, 6−10.

(38) De Maria, C.; Chiesa, I.; Morselli, D.; Ceccarini, M. R.; Bittolo Bon, S.; Degli Esposti, M.; Fabbri, P.; Morabito, A.; Beccari, T.; Valentini, L. Biomimetic tendrils by four dimensional printing bimorph springs with torsion and contraction properties based on bio-compatible graphene/silk fibroin and poly(3-hydroxybutyrate-*co*-3-hydroxyvalerate). *Adv. Funct. Mater.* **2021**, *31*, No. 2105665.

(39) Holliday, D. L.; Speirs, V. Choosing the right cell line for breast cancer research. *Breast Cancer Res.* **2011**, *13*, 215.

(40) Ceccarini, M. R.; Chiesa, I.; Ripanti, F.; Cardinali, M. A.; Micalizzi, S.; Scattini, G.; De Maria, C.; Paciaroni, A.; Petrillo, C.; Comez, L.; Bertelli, M.; Sassi, P.; Pascucci, L.; Beccari, T.; Valentini, L. Electrospun nanofibrous uv filters with bidirectional actuation properties based on salmon sperm DNA/silk fibroin for biomedical applications. *ACS Omega* **2023**, *8* (41), 38233−38242.

(41) Villarini, M.; Pagiotti, R.; Dominici, L.; Fatigoni, C.; Vannini, S.; Levorato, S.; Moretti, M. Investigation of the cytotoxic, genotoxic, and apoptosis-inducing effects of estragole isolated from fennel (Foeniculum vulgare). *J. Nat. Prod.* **2014**, *77*, 773−778.

(42) Acito, M.; Bartolini, D.; Ceccarini, M. R.; Russo, C.; Vannini, S.; Dominici, L.; Codini, M.; Villarini, M.; Galli, F.; Beccari, T.; Moretti, M. Imbalance in the antioxidant defence system and pro-genotoxic status induced by high glucose concentrations: In vitro testing in human liver cells. *Toxicol. In Vitro* **2020**, *69*, No. 105001.

(43) Lapomarda, A.; Cerqueni, G.; Geven, M. A.; et al. Physicochemical Characterization of Pectin-Gelatin Biomaterial Formulations for 3D Bioprinting. *Macromol. Biosci.* **2021**, *21*, No. 2100168.

(44) Chiesa, I.; Fortunato, G. M.; Lapomarda, A.; et al. Ultrasonic mixing chamber as an effective tool for the biofabrication of fully graded scaffolds for interface tissue engineering. *Int. J. Artif. Organs* **2019**, *42*, 586−594.

(45) Tiouitchi, G.; Ali, M. A.; Benyoussef, A.; Hamedoun, M.; Lachgar, A.; Benaissa, M.; Kara, A.; Ennaoui, A.; Mahmoud, A.;

Boschini, F.; Oughaddou, H.; El Kenz, A.; Mounkachi. From amorphous red phosphorus to a few layers of black phosphorus: a low-cost and efficient preparation process. *Mater. Lett.* **2019**, *236*, 56−59.

(46) Zhang, S.; Yang, J.; Xu, R.; Wang, F.; Li, W.; Ghufran, M.; Zhang, Y.−W.; Yu, Z.; Zhang, G.; Qin, Q.; Lu, Y. Extraordinary photoluminescence and strong temperature/angle-dependent raman responses in few-layer phosphorene. *ACS Nano* **2014**, *8*, 9590−9596.

(47) Sugai, S.; Shirotani, I. Raman and infrared reflection spectroscopy in black phosphorus. *Solid State Commun.* **1985**, *53*, 753−755.

(48) Fei, R.; Yang, L. Lattice vibrational modes and Raman scattering spectra of strained phosphorene. *Appl. Phys. Lett.* **2014**, *105*, No. 083120.

(49) Lazar, P.; Otyepková, E.; Pykal, M.; Čépe, K.; Otyepka, M. Role of the puckered anisotropic surface in the surface and adsorption properties of black phosphorus. *Nanoscale* **2018**, *10*, 8979−8988.

(50) Hanlon, D.; Backes, C.; Doherty, E.; Cucinotta, C. S.; Berner, N. C.; Boland, C.; Lee, K.; Harvey, A.; Lynch, P.; Gholamvand, Z.; Zhang, S.; Wang, K.; Moynihan, G.; Pokle, A.; Ramasse, Q. M.; McEvoy, N.; Blau, W. J.; Wang, J.; Abellan, G.; Hauke, F.; Hirsch, A.; Sanvito, S.; O'Regan, D. D.; Duesberg, G. S.; Nicolosi, V.; Coleman, J. N. Liquid exfoliation of solvent-stabilized few-layer black phosphorus for applications beyond electronics. *Nat. Commun.* **2015**, *6*, No. 8563.

(51) Liang, S.; Hasan, M. N.; Seo, J.-H. Direct observation of Raman spectra in black phosphorus under uniaxial strain conditions. *Nanomaterials* **2019**, *9*, 566.

(52) Udofia, E. N.; Zhou, W. A Guiding framework for microextrusion. additive manufacturing. *J. Manuf. Sci. Eng.* **2019**, *141*, 05080.

(53) Duty, C.; Ajinjeru, C.; Kishore, V.; Compton, B.; Hmeidat, N.; Chen, X.; Liu, P.; Hassen, A. A.; Lindahl, J.; Kunc, V. What makes a material printable? A viscoelastic model for extrusion-based 3D printing of polymers. *J. Manuf. Process.* **2018**, *35*, 526−537.

(54) Matsumoto, A.; Lindsay, A.; Abedian, B.; Kaplan, D. L. Silk fibroin solution properties related to assembly and structure. *Macromol. Biosci.* **2008**, *8*, 1006−1018.

(55) Bonatti, A. F.; Chiesa, I.; Vozzi, G.; De Maria, C. Open-source CAD-CAM simulator of the extrusion-based bioprinting process. *Bioprinting* **2021**, *24*, No. e00172.

(56) Paxton, N.; Smolan, W.; Böck, T.; Melchels, F.; Groll, J.; Jungst, T. Proposal to assess printability of bioinks for extrusion-based bioprinting and evaluation of rheological properties governing bioprintability. *Biofabrication* **2017**, *9*, No. 044107.

(57) Ribeiro, A.; Blokzijl, M. M.; Levato, R.; Visser, C. W.; Castilho, M.; Hennink, W. E.; Vermonden, T.; Malda, J. Assessing bioink shape fidelity to aid material development in 3D bioprinting. *Biofabrication* **2018**, *10*, No. 014102.

(58) Piqué, A.; Chrisey, D. B. *Direct-Write Technologies for Rapid Prototyping Applications: Sensors, Electronics, and Integrated Power Sources*; AcademicPress: NewYork, 2001.